Available online at www.sciencedirect.com

SCIENCE DIRECT®

International Journal of Heat and Fluid Flow 24 (2003) 434–443

International Journal of HEAT AND FLUID FLOW

www.elsevier.com/locate/ijhff

Prediction of the spreading mechanism of 3D turbulent wall jets with explicit Reynolds–stress closures

H.M. Lübcke, Th. Rung, F. Thiele *

Hermann-Föttinger-Institute of Fluid Mechanics, Technische Universität Berlin, Müller-Breslau-Strasse 8, D-10623 Berlin, Germany

Received 30 November 2002; accepted 26 March 2003

Abstract

The paper investigates the predictive performance of different explicit Reynolds–stress closure models when applied to the simulation of 3D wall jets. The flow is of particular interest for its remarkably large ratio of lateral to normal spreading. Experiments report that the lateral rate of spread exceeds the wall-normal rate of spread between five and nine times. This phenomenon is often vigorously misrepresented by RANS simulations. There exists some body of evidence suggesting that the large lateral spreading is due to significant amounts of turbulence-driven axial vorticity (J. Fluid Mech. 435 (2001) 305). The origin of the axial vorticity can be traced back to the anisotropy of turbulent normal stresses perpendicular to the jet axis. The present paper assess the ability of explicit stress–strain relationships to mimic the normal-stress anisotropy in 3D wall jets. It is shown that linear Boussinesq-viscosity models inevitably fail to render the spreading mechanism. Moreover, the paper argues that a physically sound modelling of 3D wall jets requires an explicit closure to include at least one quartic term.

Keywords: CFD; Turbulence modelling; Spreading rate; 3D Wall jets; Integrity-basis methods

1. Introduction

Engineering applications often feature 3D wall jets. The most prominent applications are, perhaps, the film cooling of turbine blades and the defrosting of vehicle windscreens. In both examples, the surface wetted by the jet is of major relevance to the design intent. Hence, an accurate prediction of the spreading mechanism is of crucial importance.

The discriminative spreading behaviour is a characteristic feature of the 3D wall jet. Experiments indicate that the lateral rate of spread is between five and nine times as large as the wall-normal spreading rate. Various authors, e.g. Abrahamsson (1997), Launder and Rodi (1983), Newman et al. (1972), have discussed the remarkable spreading behaviour of the 3D wall jet. Recently, Craft and Launder (2001) reported on a detailed computational investigation which aimed to identify the origin of the large lateral spreading mechanism. It was concluded, that the high lateral rate of spread can be attributed to stress-induced axial vorticity, which is generated by the anisotropy of the Reynolds-normal stresses perpendicular to the jet axis. As displayed in Fig. 1, the secondary motion enforces a lateral movement of fluid away from the symmetry plane along the bottom wall. Since the mechanism is induced by turbulence-driven secondary motion, it is closely related to the generation of stress-induced streamwise vorticity in non-circular duct flows (Rung et al., 2000). A subsidiary analysis of the non-circular duct is therefore advisable.

A general modelling framework to render the physics of the 3D wall jet might arguably be based on an implicit second-moment closure. Craft and Launder (2001) employed a complex cubic non-linear pressure–strain model and a linear pressure–strain model supplemented by corrective wall-reflection terms, to mimic the phenomenon. Such an elaborate modelling approach is, however, still unfeasible when applied to complex industrial simulations.

In contrast to Craft and Launder (2001) the present paper focuses upon explicit Reynolds-stress closures along a route suggested by Gatski and Speziale (1993), which offer a physically sound extension of the most prominent linear Boussinesq-viscosity models at modest computational effort.

---

* Corresponding author. Tel: +49-30-31422216; fax: +49-30-31421101.

E-mail address: thiele@pi.tu-berlin.de (F. Thiele).

0142-727X/03/$ - see front matter © 2003 Elsevier Science Inc. All rights reserved.
doi:10.1016/S0142-727X(03)00041-9

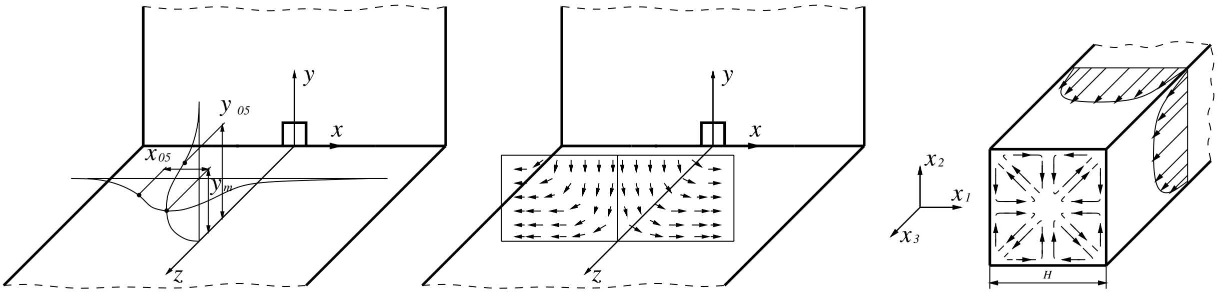

Fig. 1. Schematic of the 3D wall jet and the secondary flow in a square duct.

2. Mathematical model

The present study is confined to the analysis of an incompressible fluid based on a Reynolds-averaged approach. The governing equations for the conservation of mass and momentum read:

$$\frac{\partial \bar{u}_j}{\partial x_j} = 0, \tag{1}$$

$$\frac{\mathrm{D}\bar{u}_i}{\mathrm{D}t} = -\frac{1}{\varrho}\frac{\partial p}{\partial x_i} + \frac{\partial}{\partial x_j}\left[\nu\frac{\partial \bar{u}_i}{\partial x_j}\right] - \frac{\partial \overline{u_i'u_j'}}{\partial x_j}, \tag{2}$$

with

$$\frac{\mathrm{D}}{\mathrm{D}t} = \frac{\partial}{\partial t} + \bar{u}_j\frac{\partial}{\partial x_j}. \tag{3}$$

Here, p, ϱ, ν and $\bar{u}_i$ denote the pressure, density, viscosity and the Reynolds-averaged velocity based on Cartesian tensor notation, respectively. Supplementary to Eq. (2), a turbulence closure model for the unknown Reynolds stresses $\overline{u_i'u_j'}$ is needed to attain a closed system of equations.

Various closures featuring different degrees of complexity and predictive quality have been developed over the last decades. The most thorough implicit second-moment closures utilise individual transport equations for each component of $\overline{u_i'u_j'}$, which is computationally expensive. Industrial engineering applications predominantly employ less expensive, explicit Reynolds-stress closures. An explicit Reynolds-stress closure consists of two parts, a stress–strain relation and a background model. The stress–strain relation describes the Reynolds stresses as a function of the mean-velocity gradients and the considered unknown turbulent scalars. The background model comprises the transport equations for the considered turbulent scalars, i.e. length- and velocity-scale variables.

2.1. Background model

The most common approach is a two-equation model, based on two transport equations for the unknown scalars, i.e. the turbulence energy $k = 0.5\ \overline{u_i'u_i'}$ and the energy-dissipation rate ε. Various alternative formulations exist, e.g. $k-\omega$, $k-l$, $k-\tau$, which might yield a change of the Reynolds-stress magnitudes but do not alter the structure of the stress tensor. The active components of the Reynolds-stress tensor—in particular the degree of stress anisotropy—are primarily goverened by the employed stress–strain relation for a given strain field. The anisptropy tensor is—of course—also influenced by the background model since it globaly scales with the turbulent time scale. The latter is, however, only a scalar which carries no structural or tensorial information and thus creates no anisotropy on its own. Without the loss of generality, the present paper is thus confined to a specific low-*Re* k–ε model reported by Lien and Leschziner (1993), viz.

$$\frac{\mathrm{D}k}{\mathrm{D}t} - \frac{\partial}{\partial x_j}\left[\left(\nu + \frac{\nu_t}{Pr_k}\right)\frac{\partial k}{\partial x_j}\right] = \mathscr{P} - \varepsilon, \tag{4}$$

$$\frac{\mathrm{D}\varepsilon}{\mathrm{D}t} - \frac{\partial}{\partial x_j}\left[\left(\nu + \frac{\nu_t}{Pr_\varepsilon}\right)\frac{\partial \varepsilon}{\partial x_j}\right] = \frac{\varepsilon}{k}(C_{\varepsilon 1}\mathscr{P} - C_{\varepsilon 2}\varepsilon), \tag{5}$$

with

$$\begin{aligned}
&C_{\varepsilon 1} = 1.44 f_1, \quad C_{\varepsilon 2} = 1.92 f_2, \quad Pr_k = 1,\\
&Pr_\varepsilon = 1.3, \quad R_t = \frac{k^2}{\nu\varepsilon}, \quad R_k = \frac{\sqrt{k}n}{\nu},\\
&f_1 = 1 + \frac{\mathscr{P}}{\mathscr{P}^*}, \quad f_2 = 1 - 0.3\mathrm{e}^{-R_t^2},\\
&f_\mu = \frac{1-\mathrm{e}^{-\alpha_\mu R_k}}{1-\mathrm{e}^{-\alpha_\varepsilon R_k}}, \quad \mathscr{P} = -\overline{u_i'u_j'}S_{ij},\\
&\mathscr{P}^* = \frac{f_2 C_{\varepsilon 2} k^{1.5}}{C_{\varepsilon 1} L_\varepsilon}\mathrm{e}^{-\alpha_d R_k^2},\\
&L_\varepsilon = \kappa\overline{c_\mu}^{(-0.75)} n(1-\mathrm{e}^{-\alpha_\varepsilon R_k}),\\
&\overline{c_\mu} = 0.09, \quad \alpha_d = 0.0022,\\
&\alpha_\varepsilon = 0.263, \quad \alpha_\mu = 0.016.
\end{aligned} \tag{6}$$

2.2. Explicit Reynolds-stress closure

The most popular representative of an explicit Reynolds-stress closure is the well known linear Boussinesq-viscosity model (BVM), viz.

$$b_{ij} = -\overline{c_\mu} T_t S_{ij}. \tag{7}$$

In Eq. (7), $b_{ij} = (\overline{u_i u_j} - \frac{2}{3}k\delta_{ij})/2k$ is the Reynolds-stress anisotropy tensor and $S_{ij} = (\partial \bar{u}_i/\partial x_j + \partial \bar{u}_j/\partial x_i)/2$ and $T_t = k/\varepsilon$ denote the strain-rate tensor and the turbulent time scale respectively. The main reason for the popularity of the BVM is the similarity to the definition of viscous stresses, which grossly simplifies the numerical implementation.

According to the representation theory (cf. Spencer and Rivlin, 1959), the linear BVM (7) is a first-order truncation of a complete non-linear relationship between the Reynolds-stress anisotropy tensor and the velocity gradients, viz.

$$b_{ij}(s_{kl}, w_{kl}) = \sum_\lambda \alpha_\lambda T^\lambda_{ij}, \tag{8}$$

with

$$T^\lambda_{ij} = T^\lambda_{ij}(s_{kl}, w_{kl}), \tag{9}$$

with $w_{ij} = T_t(\partial \bar{u}_i/\partial x_j - \partial \bar{u}_j/\partial x_i)/2$ and $s_{ij} = T_t S_{ij}$. The representation theory identifies the relevant generators T^λ_{ij} by means of integrity-basis methods. The integrity basis is the set of all independent matrix products of a given group of tensors (i.e. s_{ij} and w_{ij}). Spencer and Rivlin (1959) proved that for $b_{ij}(s_{kl}; w_{kl})$, the integrity basis contains only 10 matrix products (generators):

$$\begin{aligned}
T^1_{ij} &= s_{ij},\\
T^2_{ij} &= s_{ik}w_{kj} - w_{ik}s_{kj},\\
T^3_{ij} &= s_{ik}s_{kj} - \tfrac{1}{3}\eta_1\delta_{ij},\\
T^4_{ij} &= w_{ik}w_{kj} - \tfrac{1}{3}\eta_2\delta_{ij},\\
T^5_{ij} &= w_{ik}s_{kl}s_{lj} - s_{ik}s_{kl}w_{lj},\\
T^6_{ij} &= w_{ik}w_{kl}s_{lj} + s_{ik}w_{kl}w_{lj} - \tfrac{2}{3}\eta_4\delta_{ij},\\
T^7_{ij} &= w_{ik}s_{kl}w_{lq}w_{qj} - w_{ik}w_{kl}s_{lq}w_{qj},\\
T^8_{ij} &= s_{ik}w_{kl}s_{lq}s_{qj} - s_{ik}s_{kl}w_{lq}s_{qj},\\
T^9_{ij} &= w_{ik}w_{kl}s_{lq}s_{qj} + s_{ik}s_{kl}w_{lq}w_{qj} - \tfrac{2}{3}\eta_5\delta_{ij},\\
T^{10}_{ij} &= w_{ik}s_{kl}s_{lq}w_{qp}w_{pj} - w_{ik}w_{kl}s_{lq}s_{qp}w_{pj}.
\end{aligned} \tag{10}$$

The associated 10 coefficients α_λ are functions of the irreducible invariants of the integrity basis (10), i.e.

$$\begin{aligned}
&\eta_1 = s_{ik}s_{ki}, \quad \eta_2 = w_{ik}w_{ki},\\
&\eta_3 = s_{ik}s_{kj}s_{ji}, \quad \eta_4 = s_{ik}w_{kj}w_{ji},\\
&\eta_5 = s_{ik}s_{kl}w_{lj}w_{ji}.
\end{aligned} \tag{11}$$

Unfortunately, the representation theory provides no specific information on the associated coefficients α_λ. In order to evaluate the coefficients α_λ, Gatski and Speziale (1993) developed an explicit solution to the implicit algebraic-stress model as proposed by Rodi (1976):

$$\begin{aligned}
gb_{ij} = A_1 s_{ij} - A_2(b_{ik}w_{kj} - w_{ik}b_{kj}) + A_3\big(&b_{ik}s_{kj}\\
&+ s_{ik}b_{kj} - \tfrac{2}{3}(b_{mk}s_{km})\delta_{ij}\big),
\end{aligned} \tag{12}$$

with

$$g = C_1 - 2(b_{ik}s_{ki}) - 1, \quad A_1 = \tfrac{1}{2}C_2 - \tfrac{2}{3},$$
$$A_2 = \tfrac{1}{2}C_4 - 1, \quad A_3 = \tfrac{1}{2}C_3 - 1.$$

C_i denote the constants of the linear pressure-strain correlation model, which have been substituted into the ASM, viz.

$$\begin{aligned}
\Phi_{ij} = -2C_1\varepsilon b_{ij} + C_2 k S_{ij} + C_3 k\big(&b_{il}S_{jl} + b_{jl}S_{il} - \tfrac{2}{3}b_{ml}S_{ml}\delta_{ij}\big)\\
&+ C_4 k(b_{il}W_{jl} + b_{jl}W_{il}).
\end{aligned} \tag{13}$$

The present paper employs the coefficients developed by Rung et al. (1999), i.e. $C_1 = 2.5$, $C_2 = 0.39$, $C_3 = 1.25$ and $C_4 = 0.45$. Introducing the expressions for the anisotropy tensor (8) and integrity basis (10) into the ASM equation (12), the coefficients α_λ are determined from the solution of the emerging linear 10×10 equation system (Gatski and Speziale, 1993). The resulting complete explicit algebraic-stress model (EASM) generally involves 9 rather complex, non-zero coefficients α_λ. The model is thus quite cumbersome and of limited use.

2.3. Projection method

Recently, Jongen and Gatski (1998) introduced a projection method, which enables an approximate solution based on an arbitrary selection of generators. The method projects the ASM (12) into the chosen integrity basis, which yields a linear equation system to determine the unknown coefficients of the polynomial expansion. If the selected basis conforms with the complete integrity basis (10), the solution of Gatski and Speziale (1993) is recovered. Any reduced integrity basis provides an approximate solution. The projection method fails if the generators of the integrity basis are linearly dependent. It is thus advantageous to compile the basis as a subset of the complete integrity basis (10). Generally, the specific basis that is produced should render the relevant flow physics at modest computational demands.

In 2D mean flows, the integrity basis (10) collapses to only three independent generators T^1_{ij}, T^2_{ij} and T^3_{ij}. A robust explicit-stress closure that reconciles enhanced predictive capabilities with moderate computational expenses consists of a projection of these independent generators. Introducing $\alpha_0 b_{ij} = \sum_{n=1}^{3}\alpha_n T^n_{ij}$ into the ASM (12) and subsequently multiplying the resulting equation with the each of the considered generators, three linear equations result from after taking the trace of each equation. The resulting 3×3 system for the specification of the unknown coefficients $\alpha_{1,\ldots,3}$ reads

$$\begin{aligned}
&[g(M_{nm})^{\mathrm{T}} + 2A_2(M^w_{nm})^{\mathrm{T}} - 2A_3(M^s_{nm})^{\mathrm{T}}]\alpha_n\\
&\quad = [M^p_{nm}]^{\mathrm{T}}\alpha_n = \alpha_0 A_1 L_m
\end{aligned} \tag{14}$$

with $\alpha_0 = det(M^p_{mn})$, $n, m \in (1, 2, 3)$ and

$$M_{nm} = T^n_{ik} T^m_{ki}, \quad M^s_{nm} = T^n_{ik} s_{kj} T^m_{ji},$$
$$M^w_{nm} = T^n_{ik} w_{kj} T^m_{ji}, \quad L_m = s_{ik} T^m_{ki}.$$

It should be noted that Eq. (14) still includes higher-order invariants which can be further simplified by restricting our interest to 2D mean flow (Gatski and Speziale, 1993). The respective 2D solution of the equation system (14) is usually cast into the standard form of a quadratic EASM, viz.

$$\begin{aligned} b_{ij} &= -c_\mu \left(s_{ij} + \beta_2 \{ s_{ik} w_{kj} - w_{ik} s_{kj} \} - \beta_3 \left\{ s_{ik} s_{kj} - \tfrac{1}{3} \eta_1 \delta_{ij} \right\} \right), \\ \beta_2 &= -A_2/g, \;\; \beta_3 = -2A_3/g, \\ c_\mu &= \frac{-A_1 g}{g^2 - \frac{2}{3} A_3^2 \eta_1 - 2A_2^2 \eta_2}. \end{aligned} \tag{15}$$

3. Numerical scheme

The numerical procedure ELAN (Xue, 1998) consists of a semi-structured, multi-block method It is based on the fully conservative approximation of the 3D Reynolds-averaged Navier–Stokes equations within general curvelinear coordinates. The procedure employs a cell-centered, co-located storage arrangement for all transport properties. Diffusion terms are approximated using second-order central differences, whereas advective fluxes are approximated using higher-order monotonicity preserving schemes. The latter are applied in scalar form by means of a deferred-correction procedure. The odd–even decoupling problem of the cell-centered scheme is suppressed with a fourth-order artificial dissipation pressure term in the continuity equation. The solution is iterated to convergence using a pressure-correction approach. Various turbulence-transport and subgrid scale models are implemented based on the apparent pressure/viscosity principle. In order to reduce the computational effort, the solver is parallelised by means of a domain-decomposition method.

4. Modelling of turbulent-secondary motion

The accurate prediction of stress-induced streamwise vorticity is crucial for the successful prediction of 3D wall jets. Confining our interest to the prediction of turbulent-secondary motion, it is instructive to briefly elucidate the performance of the quadratic baseline EASM (15) in simple channel flows and in non-circular duct flows (cf. Fig. 1)—the latter also features turbulence generated streamwise vorticity.

Table 1
Incompressible (homogeneous) shear flow $\bar{u}_1(x_2)$: Performance of the present EASM in comparison to DNS data reported by Kim et al. (1987) and Rogers et al. (1986) for two different shear rates $S = k/\varepsilon |d\bar{u}_1/dx_2|$

	$S = 3.3$		$S = 5.7$	
	EASM	DNS	EASM	DNS
b_{11}	0.180	0.179	0.215	0.215
b_{22}	−0.130	−0.127	−0.155	−0.153
b_{33}	−0.050	−0.052	−0.060	−0.062
b_{12}	−0.158	−0.143	−0.157	−0.158

The first example of the present paper is devoted to the models ability to accurately mimic the degree of stress-anisotropy in a simple 2D turbulent channel flow. Table 1 illustrates the fair predictive performance of the present EASM. Whilst not crucial for simple shear flows, the predictive performance displayed in the channel flow example will have serious implication on the prediciton of turbulence-driven secondary motion, which predominantly hinges on an accurate prediction of normal-stress anisotropy. It should be noted, that the the cubic and quartic terms are irrelevant for the channel flow since they vanish in simple uni-directional shear flows.

4.1. Fully-developed square duct

It was outlined by Rung et al. (2000) that both the magnitude and the orientation of the turbulent-secondary motion in a non-circular duct flow are governed by the rapid part of the linear pressure–strain model (13). Due to the fully developed state of the flow, the velocity gradients normal to the walls dominate the velocity-gradient tensor. As in 2D flows, only the first three generators of the integrity basis are independent. Thus, a quadratic model should be sufficient to render the turbulent physics. Substituting the Reynolds stress tensor by the related quadratic EASM expression (15) into the momentum equation (2), one obtains an equation for the secondary motion, i.e.

$$\begin{aligned} \frac{\partial \bar{u}_1}{\partial t} + \bar{u}_1 \frac{\partial \bar{u}_1}{\partial x_1} + \bar{u}_2 \frac{\partial \bar{u}_1}{\partial x_2} = -\frac{1}{\bar{\varrho}} \frac{\partial \bar{p}}{\partial x_1} - \frac{2}{3} \frac{\partial}{\partial x_1} \left(k + c_\mu k \frac{A_3}{g} \eta_1 \right) \\ + 2 \frac{\partial}{\partial x_1} \left(2 c_\mu k \frac{A_3 - A_2}{g} s_{13}^2 \right) \\ + 2 \frac{\partial}{\partial x_2} \left(2 c_\mu k \frac{A_3 - A_2}{g} s_{13} s_{23} \right). \end{aligned} \tag{16}$$

Obviously, the secondary flow hinges on the coefficient difference $A_3 - A_2 = \frac{1}{2}(C_3 - C_4)$ which vanishes for a linear BVM. Fig. 2 compares the predicted secondary flow patterns obtained from the linear BVM (7) and the quadratic EASM (15) for the fully-developed square duct flow at $Re_H = 4200$. The numerical grid consists of $72 \times 72 \times 10$ nodes, with $Y^+ \approx 0.3$. The linear model predicts no secondary motion, whereas the quadratic EASM features a significant amount of secondary flow. The impact of the secondary motion to the primary velocity ($\bar{u}_3$) is insignificant, hence both models return similar primary velocities.

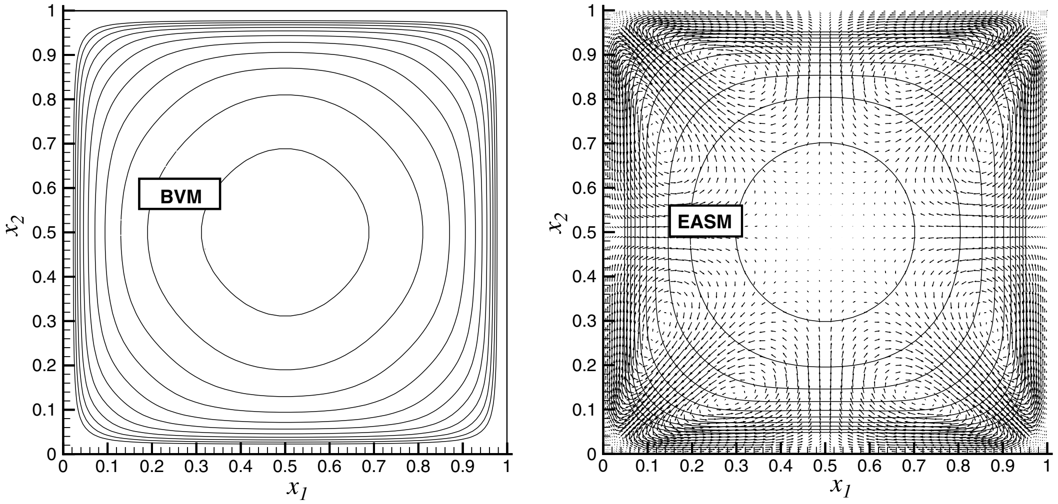

Fig. 2. Turbulent square duct at $Re_H = 4200$ (Cheesewright et al., 1990): Primary-velocity isolines obtained from a Boussinesq-viscosity model (left) and a quadratic explicit algebraic-stress model (right) with secondary-flow vectors.

The latter is more obvious from the comparison of primary and secondary velocity profiles with experiments of Cheesewright et al. (1990) displayed in Fig. 3. The figure confirms, that the influence of the secondary flow is rather weak, thus, linear and quadratic model are in close agreement with the experimental data. However, the linear model completely fails to predict the secondary flow whilst the quadratic shows a good qualitative agreement with the experiment. The orientation of the secondary flow is correctly captured, only the magnitude is under predicted at some positions. As outlined by Rung et al. (2000), the higher-order generators vanish in this flow. Hence, the quartic model yields the same result as the quadratic one.

4.2. 3D wall jet

The gross features of the velocity gradients in a 3D wall jet resemble those of the aforementioned square duct. The symmetry plane of both examples is dominated by the velocity gradients in the normal and lateral directions (cf. Fig. 1). However, a closer inspection of the two examples reveals two fundamental differences. As opposed to the fully developed state of the duct flow, the 3D wall jet features a significant primary velocity gradient along the jet axis. Moreover, the secondary flow in the 3D wall jet has a prominent impact on the development of the primary motion. The latter is of particular relevance, since the secondary flow of the 3D wall jet is indeed of opposite orientation. Contrary to the square-duct example, the secondary motion pushes the fluid away from the symmetry plane along the wall (cf. Fig. 1). A quadratic stress–strain relation, which captures the secondary motion in a non-circular duct, will thus return an utterly wrong prediction when applied to the 3D wall jet problem. In the remainder of the paper, results will be reported for a generic wall jet discharged through a square orifice. The investigated Reynolds number based on the width d of the orifice and the bulk velocity is $Re_d = 60\,000$. The computational domain covers $75d$ in lateral, $50d$ in normal and $100d$ in downstream direction. The employed numerical grid consists of $100 \times 70 \times 150$ nodes. It was derived from initial test with a 2D wall jet and subjected to a subsequent grid-refinement for the final 3D jet case. The refinement process did address resolution aspects and the impact of the size of the physical domain. The final grid displayed no further improvements when the grid resolution was increased.

Fig. 4 depicts the predictive failures of the quadratic EASM (15) and the linear BVM (7) in the 3D wall-jet problem. The BVM predicts no secondary motion and a small amount of lateral spread. The stress-anisotropy induced vorticity is not captured due to the isotropic nature of the BVM. The almost circular isolines show no preferred direction. Likewise, the ratio of the lateral-to-normal rate of spread is close to unity. As outlined above, the calibration of the pressure–strain model with regards to the square-duct example yields the wrong secondary motion due to its rigid alignment to 2D mean flow situations. The secondary motion erroneously pushes the fluid towards the symmetry plane and thereby attenuates the lateral spreading. The intensity of the secondary motion is small. Hence, the influence on the primary flow is minor and the corresponding isolines show only a weak inflection towards the wall-normal direction.

The conventional EASM is confined to linear pressure-strain models omitting corrective wall-reflection terms. Thus, the linear formulations suggested by Craft

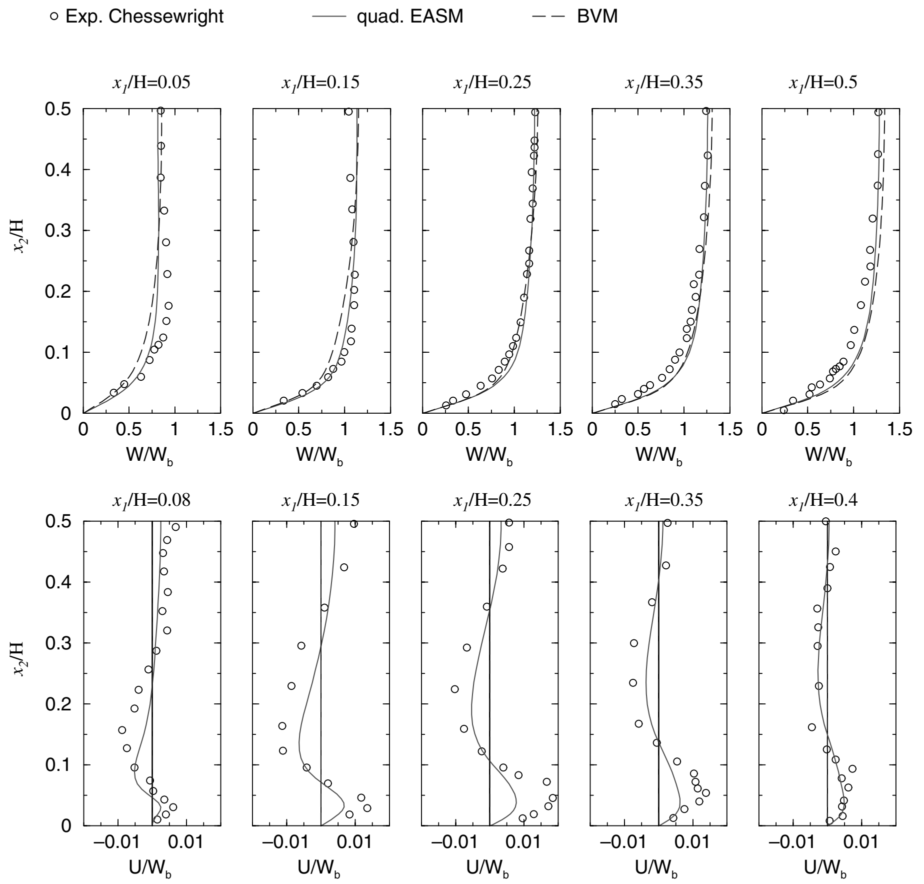

Fig. 3. Turbulent square duct at $Re_H = 4200$ (Cheesewright et al., 1990): Comparison of primary (top) and secondary velocity (bottom) in with experimental data from Cheesewright et al. (1990).

and Launder (2001) cannot be used. The present approach aims to mimic the spreading mechanism of the 3D wall jet via the inclusion of additional generators supplementary to the quadratic baseline formulation (15).

The axial vorticity is primarily induced through the normal-stress anisotropy in response to principal strains. Since the normal-stress anisotropy due to a primary shear is aligned to the even-order terms of the EASM, the quartic generators of the integrity basis (10) are most appropriate to model the phenomenon. The additional generators should, of course, not affect the performance of the quadratic baseline model in 2D mean flows. Hence, it is advantageous to consider only generators which vanish in 2D flows. The accordingly modified quartic generators read

$$\begin{aligned} T_{ij}^{7'} &= T_{ij}^{7} + \tfrac{1}{2}\eta_2 T_{ij}^{(2)}, \\ T_{ij}^{8'} &= T_{ij}^{8} - \tfrac{1}{2}\eta_1 T_{ij}^{(2)}, \\ T_{ij}^{9'} &= T_{ij}^{9} - \eta_2 T_{ij}^{(3)}. \end{aligned} \tag{17}$$

With respect to the co-ordinate system displayed in Fig. 1, the non dimensional strain-rate and vorticity tensors of the 3D wall jet reduce in first order towards:

$$s_{ij} = \begin{bmatrix} -C & 0 & A \\ 0 & 0 & B \\ A & B & C \end{bmatrix} \tag{18}$$

and

$$w_{ij} = \begin{bmatrix} 0 & 0 & -A \\ 0 & 0 & -B \\ A & B & 0 \end{bmatrix}. \tag{19}$$

The corresponding quartic generators (17) follow from

$$\begin{aligned} T_{ij}^{7'} &= \begin{bmatrix} 0 & 0 & -A^2BC \\ 0 & 0 & A^2BC \\ -A^2BC & A^2BC & 0 \end{bmatrix}, \\ T_{ij}^{8'} &= \begin{bmatrix} 0 & 0 & A^2BC \\ 0 & -2B^2C^2 & -BCD^2 \\ A^2BC & -BCD^2 & 2B^2C^2 \end{bmatrix}, \\ T_{ij}^{9'} &= \begin{bmatrix} \tfrac{4}{3}B^2C^2 & -A^2BC & -A^2BC \\ -A^2BC & -\tfrac{2}{3}B^2C^2 & A^2BC \\ -A^2BC & A^2BC & -\tfrac{2}{3}B^2C^2 \end{bmatrix} \end{aligned} \tag{20}$$

with $D^2 = (A^2 + C^2)$.

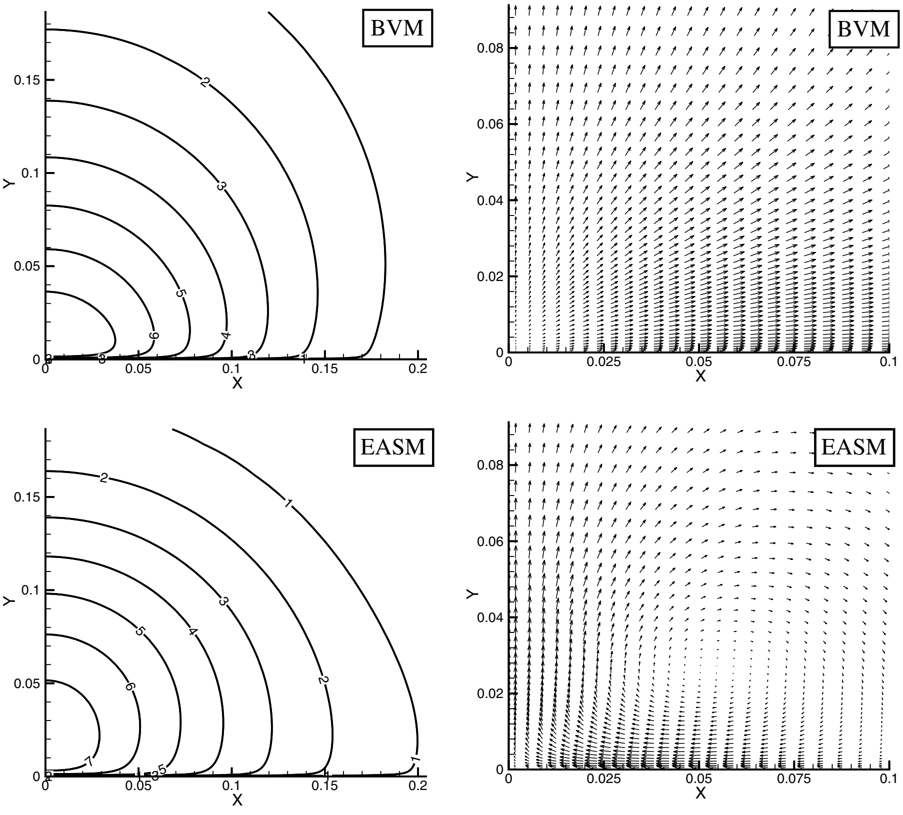

Fig. 4. 3D wall jet at $Re_d = 60000$ (Abrahamsson, 1997): Isolines of the primary velocity (left) and secondary flow (right) obtained from the linear Boussinesq-viscosity model (top row) and the quadratic explicit algebraic-stress model (bottom row).

$T_{ij}^{7'}$ includes no contribution from the normal-stress components and is therefore unable to capture the anisotropy induced secondary motion of the 3D wall jet. Both $T_{ij}^{8'}$ and $T_{ij}^{9'}$ feature the aspired normal-stress anisotropy. Due to its sparse nature, $T_{ij}^{8'}$ has been chosen to model the 3D wall jet in the present paper.

In view of a more general model, it is beneficial to include an additional cubic generator, i.e. T_{ij}^{5}. The cubic term improves the predictive performance in flows featuring curvature induced variations of turbulent shear, e.g. the rotating pipe flow, but has almost no influence on the wall-jet predictions. Moreover, T_{ij}^{5} also vanishes in 2D flows and does not alter the existing 2D model. The coefficients of explicit-stress closure are again determined by the projection method. In order to preserve the simplicity of the quadratic model, only the leading-order terms (invariants) are considered in the equation system which is used to determine the coefficients $\alpha_{1\ldots5}$. In particular, higher-order invariants, e.g. η_3, η_4, are neglected. Projecting the ASM (12) into the 5-generator basis T_{ij}^{1}, T_{ij}^{2}, T_{ij}^{3}, T_{ij}^{5} and $T_{ij}^{8'}$ and restricting our interest to the leading-order terms, the explicit stress–strain relation finally reads:

$$
\begin{aligned}
b_{ij} &= -2c_\mu T_t\big(S_{ij} + \beta_2 T_t\{S_{ik}W_{kj} - W_{ik}S_{kj}\} \\
&\quad - \beta_3 T_t\{S_{ik}S_{kj} - \tfrac{1}{3}S_{kq}S_{qk}\delta_{ij}\} + \beta_5 T_t^2\{W_{ik}S_{kl}S_{lj} \\
&\quad - S_{ik}S_{kl}W_{lj}\} + \beta_8 T_t^3\{S_{ik}W_{kl}S_{lq}S_{qj} - S_{ik}S_{kl}W_{lq}S_{qj} \\
&\quad - \tfrac{1}{2}S_{pm}S_{mp}[S_{ik}W_{kj} - W_{ik}S_{kj}]\}\big), \\
c_\mu &= \frac{-A_1 g}{g^2 - \frac{2}{3}A_3^2\eta_1 - 2A_2^2\eta_2}, \\
\beta_2 &= -A_2/g, \quad \beta_3 = -2A_3/g, \\
\beta_5 &= \frac{-6A_2(A_3 - A_2\sqrt{-\eta_2/\eta_1})}{-2g^2 + A_3^2\eta_1 + A_2^2\eta_2}, \quad \beta_8 = C^{8'}\frac{-6A_2}{\eta_1 g}.
\end{aligned}
\tag{21}
$$

The introduction of the additional coefficient $C^{8'}$ deserves further attention. It aims to facilitate an improved modelling of the wall jet, in particular the correct orientation of the secondary motion. In the present model, the latter is achieved by setting $C^{8'} = -1$. The approach might be considered as a violation of the modelling rationale. It should, however, be noted that the adopted projection method already represents

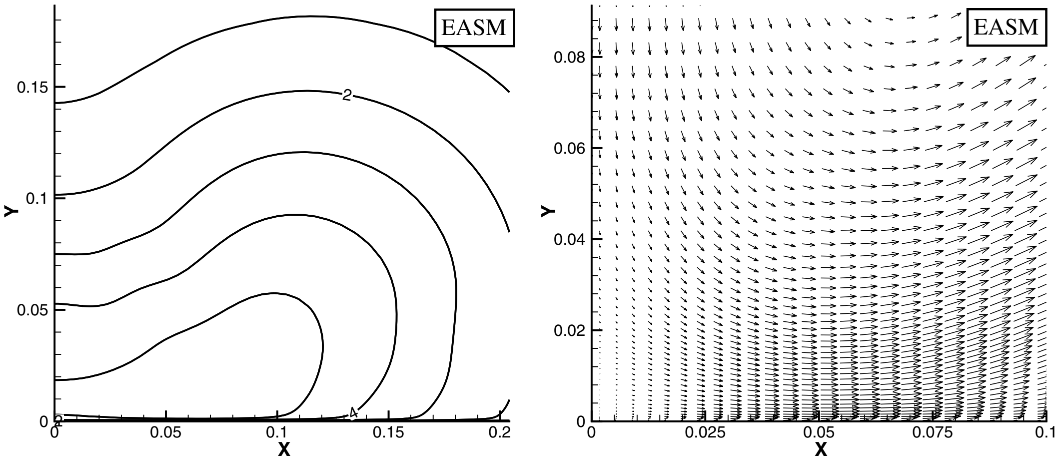

Fig. 5. 3D wall jet at $Re_d = 60000$ (Abrahamsson, 1997): Isolines of the primary velocity (left) and secondary flow (right) obtained from the quartic EASM (21).

an approximate solution. Furthermore, the projection method generally returns complex coefficients in conjunction with higher-order generators, which might become singular and require a simplification. The latter is achieved by removing high-order invariants from the matrices. Therefore the rigorous concept of the EASM is already broken before the constant $C^{8'}$ is introduced.

4.3. Results of the quartic model

The predictive response of the suggested quartic stress–strain relation (21) is depicted by Fig. 5. A comparison with Fig. 4 reveals that the quartic model is clearly superior to the traditional alternatives.

As indicated by Fig. 5, the secondary motion displays the desired orientation which is opposite of the square duct example. Driven by the stress induced secondary motion, the fluid travels down the symmetry plane and augments the lateral spreading along the wall. A clear flattening of the isolines proves that the predicted lateral rate of spread exceeds the normal rate of spread. Whilst the higher lateral spreading corresponds to experimental findings, the quartic models shows a bulging of the isolines away from the symmetry plane, which is not reported by experiments. The predicted secondary flow has the correct orientation, however, the model shows a pronounced vortex-like structure. In contrast to the experiment, the quartic models returns a more confined secondary flow regime, predicting the center of the vortex in close proximity to the symmetry plane. Accordingly, an upward motion is introduced which deforms the isolines.

A classical feature of the wall jet is the approach of a self-preserving state downstream of the development region. Fig. 6 displays that all models under investigation, i.e. BVM, quadratic and quartic EASM, predict a self-similar behaviour of the flow downstream of $z/d \approx 50$. Fig. 7 reveals that the primary velocity of the 3D wall jet is significantly affected by the evolution of the secondary motion. The axial velocity in direction of the jet axis is reduced by means of the strong lateral spreading. The quartic EASM is the only model which predicts an enhancement of the lateral spread due to turbulent-secondary motion. Accordingly, it returns the most pronounced attenuation of the primary velocity

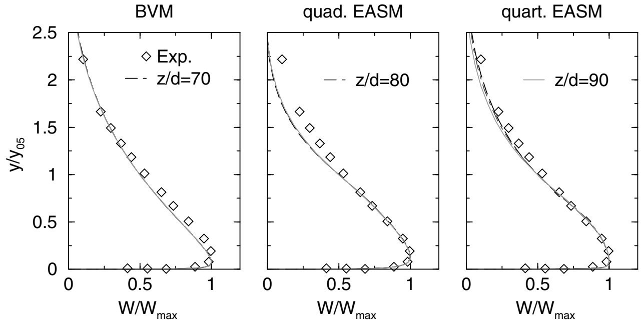

Fig. 6. 3D wall jet at $Re_d = 60000$ (Abrahamsson, 1997): Self-similar primary velocity profiles normal to the wall at different streamwise positions ($z/d = 70$, $z/d = 80$, $z/d = 90$).

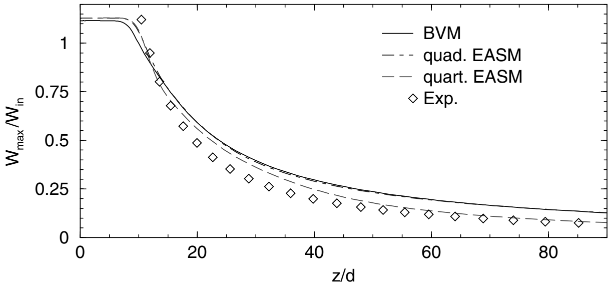

Fig. 7. 3D wall jet at $Re_d = 60000$ (Abrahamsson, 1997): Evolution of the axial mean-flow velocity maxima in the symmetry plane.

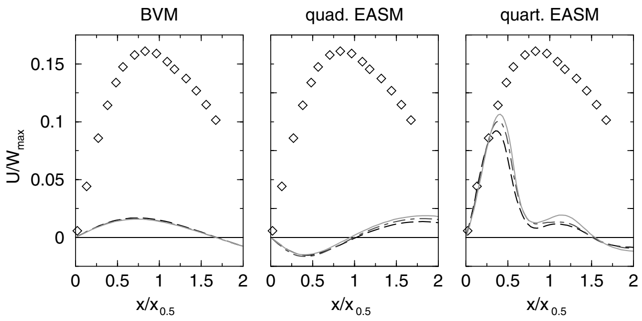

Fig. 8. 3D wall jet at $Re_d = 60000$ (Abrahamsson, 1997): Lateral velocity lateral to wall at y_m (legend as Fig. 6).

when the jet travels downstream. With attention restricted to the self-similar regime ($z/d > 60$), the agreement between the quartic model and experiments reported by Abrahamsson (1997) is fair.

A more detailed comparison of the predicted secondary flow is obtained from the normalised lateral velocity profiles illustrated by Fig. 8. While the linear and the quadratic models display only a weak secondary motion, the quartic model agrees well with the measurements near the symmetry plane. The magnitude of the predicted secondary velocity obtained from the quartic model is about eight times larger than the result of the linear model. However, the predicted secondary motion collapses aft of the lateral half-width, which yields a substantially lower spreading rate when compared to the experiment. Moreover, the quartic EASM shows a slight deterioration from the self-similar state. At all three positions displayed in Fig. 8, the lateral velocity profiles of the EASM agree in their shape but feature a slight variation of the amplitude. In contrast, the profiles of primary velocity illustrated by Fig. 6 depict a more satidfactory self-similarity. Table 2 summarises the computed spreading rates in comparison to Abrahamsson's (1997) experimental data and second-moment closure results reported by Craft and Launder (2001). The quartic model still under-predicts the experimental spreading ratio by 50%. The spreading ratio obtained from the quartic model is, however, three times larger than the ratio obtained by the traditional BVM. In contrast to the present EASM, the non-linear second-moment closure suggested by Craft et al. significantly over-predicts the spreading ratio.

Table 2
3D turbulent wall jet at $Re_d = 60\,000$ (Abrahamsson, 1997): Comparison of predicted lateral and normal spreading rates obtained from the various EASM with experiments of Abrahamsson (1997) and full second-moment transport closures reported by Craft and Launder (2001)

	$\partial y_{0.5}/\partial z$	$\partial x_{0.5}/\partial z$	$x'_{0.5}/y'_{0.5}$
Exp. Abrahamsson (1997)	0.065	0.320	4.94
RSTM (IP, w/o wall reflection)	0.081	0.079	0.97
RSTM (IP, with wall reflection)	0.053	0.814	15.3
RSTM (TCL)	0.060	0.510	8.54
linear BVM	0.075	0.061	0.81
quadratic EASM	0.077	0.065	0.84
quartic EASM	0.064	0.165	2.57

5. Concluding remarks

The focal point of the paper is the computational modelling of the spreading mechanism of a 3D wall jet by means of an explicit algebraic stress model. The modelling approach is based on two building-block flows which are both driven by turbulent-secondary motion, i.e. the fully developed square-duct and the 3D wall jet. The comparative analysis of these two flows reveals that the 3D wall jet is beyond the predictive realms of traditional linear and quadratic stress–strain relations. The paper argues that a necessary prerequisite for the accurate simulation of the spreading mechanism featured by 3D wall jets is a decoupling of the principal axes of the Reynolds-stress- and velocity-gradient tensors.

The primary objective of the presented quartic EASM is to mimic the correct structure of the Reynolds-stress tensor for the wall jet while retaining the baseline performance of the quadratic formulation. The latter is achieved by the inclusion of quartic terms which vanish in 2D mean flow situations. The adopted approach demonstrates the suitability of the projection method for the introduction of a novel qualitative feature to the modelling frame. The suggested EASM captures the correct secondary motion for both the square-duct flow and the 3D wall jet. For the 3D wall jet, the quartic explicit-closure achieves the same overall predictive accuracy as an elaborate second-moment closure (Craft and Launder, 2001).

References

Abrahamsson, H., 1997. On turbulent wall jets. PhD thesis, Dept. of Thermo and Fluid Dynamics, Chalmers University of Technology, Göteborg, Sweden.

Cheesewright, R., McGrath, G., Petty, D., 1990. LDA measurements of turbulent flow in a duct of square cross section at low Reynolds number. Aeronautical Eng. Dept. Rep. ER 1011, Queen Mary Westfield College, Uni. London, UK.

Craft, T.J., Launder, B.E., 2001. On the spreading mechanism of the three-dimensional turbulent wall jet. J. Fluid Mech. 435, 305.

Gatski, T.B., Speziale, C.G., 1993. On explicit algebraic stress models for complex turbulent flows. J.Fluid Mech. 254, 59.

Jongen, T., Gatski, T.B., 1998. General explicit algebraic relations and best approximation for three-dimensional flows. Int. J. Eng. Sci. 36, 739.

Kim, J., Moin, P., Moser, R., 1987. Turbulence statistics of a fully developed channel flow at low Reynolds number. J. Fluid Mech. 177, 133.

Launder, B.E., Rodi, W., 1983. The turbulent wall jet. Annu. Rev. Fluid Mech. 15, 429.

Lien, F.S., Leschziner, M.A., 1993. Computational modelling of 3d turbulent flow in s–diffuser and transition ducts. In: Engineering Turbulence Modelling and Experiments, 2. Elsevier, Amsterdam, p. 217.

Newman, B.G., Patel, R.P., Savage, S.B., Tjio, H.K., 1972. Three-dimensional wall jet originating from a circular orifice. Aeronaut. Q. 23, 187.

Rodi, W., 1976. A new algebraic relation for calculating the Reynolds stresses. ZAMM 56, T219.

Rogers, M.M., Moin, P., Reynolds, W.C., 1986. The structure and modelling of hydrodynamic and passive scalar field in homogeneous turbulent shear flow. Tech. Rep. TR TF–25, Thermosciences Division, Dept. Mech. Engineering, Stanford University, CA.

Rung, T., Lübcke, H.M., Xue, L., Thiele, F., Fu, S., 1999. Assessment of explicit algebraic Reynolds-stress models in transonic flows. In: Engineering Turbulence Modelling and Experiments, 4. Elsevier, Amsterdam, p. 659.

Rung, T., Lübcke, H.M., Thiele, F., Fu, S., Wang, C., Guo, Y., 2000. A turbulence closure model constraint derived from stress-induced secondary flow. AIAA J. 38 (9), 1756.

Spencer, A.J.M., Rivlin, R.S., 1959. The theory of matrix polynomials and its application to the mechanics of isotropic continua. Arch. Rational Mech. Anal. 2, 309.

Xue, L., 1998. Entwicklung eines effizienten paralellen Lösungsalgorithmus zur numerischen Simulation komplexer turbulenter Strömungen. PhD Thesis, TU Berlin.